ELSEVIER

Fusion Engineering and Design 60 (2002) 527–546

Fusion Engineering and Design

www.elsevier.com/locate/fusengdes

Prediction of material erosion and lifetime during major plasma instabilities in tokamak devices

Ahmed Hassanein *

Argonne National Laboratory, 9700 South Cass Avenue, Argonne, IL 60439, USA

Abstract

Surface and structural damage to plasma-facing components due to the frequent loss of plasma confinement remains a serious problem for the tokamak reactor concept. The deposited plasma energy during major disruptions, edge-localized modes (ELMs), and vertical displacement events (VDEs) causes significant surface erosion, possible structural failure, and frequent plasma contamination. Surface damage consists of vaporization, spallation, and liquid splatter of metallic materials. Structural damage includes large temperature increases and high thermal stresses in structural materials and at the interfaces between surface coatings and structural members. To evaluate the lifetimes of plasma-facing materials and nearby components and to predict the various forms of damage that they experience, comprehensive models (contained in the HEIGHTS computer simulation package) are developed, integrated self-consistently, and enhanced. Splashing mechanisms such as bubble boiling and various liquid magnetohydrodynamic (MHD) instabilities and brittle destruction mechanisms of nonmelting materials can be serious erosion mechanisms and are being studied in detail. The ejected macroscopic particles (MPs) will interact with incoming plasma particles and with the vapor cloud above the surface. Therefore, the dynamic behavior of MPs in the vapor cloud and their influence on total erosion rate is important. Results of self-consistent MHD calculations are presented in which the dynamics of both the vapor cloud and MP interaction are coupled with incoming plasma ions and electrons from the scrape-off layer during a disruption. The design requirements and implications of plasma facing and nearby components are discussed, along with recommendations to mitigate and reduce the effects of plasma instabilities on reactor components. Published by Elsevier Science B.V.

Keywords: Erosion; Disruptions; Melting; Splashing; Vapor shielding; HEIGHTS package

1. Introduction

Interaction of powerful plasma and particle beams (power densities up to hundreds of GW m^{-2} and time duration up to tens of ms) with various materials significantly damages exposed target surfaces and nearby components. Investigation of material erosion and damage due to intense energy deposition on target surfaces is essential for many applications, space studies; study of the earth surface interaction with colliding asteroids and comets, creation of new sources of radiation; high-energy physics applications; thermonuclear and inertial fusion studies, etc. Experimental and theoretical activities in this field

* Tel.: +1-630-252-5889; fax: +1-630-252-3250.
E-mail address: hassanein@anl.gov (A. Hassanein).

0920-3796/02/$ - see front matter Published by Elsevier Science B.V.
PII: S0920-3796(02)00008-X

move toward the common goal of achieving a better understanding of the physics phenomena and material properties of various plasma–surface interactions under extreme conditions of high temperature and pressure. An important application of this understanding is in future tokamak fusion devices during plasma interaction with plasma-facing materials (PFMs).

Damage to plasma-facing and nearby components as a result of various plasma instabilities that cause loss of plasma confinement remains a major obstacle to a successful tokamak reactor concept. Plasma instabilities can take various forms, such as major disruptions, which include both thermal and current quench (sometimes producing runaway electrons); edge-localized modes (ELMs), and vertical displacement events (VDEs). The extent of the damage depends on the detailed physics of the disrupting plasma, the physics of plasma–material interactions, and the design configuration of plasma-facing components (PFCs) [1]. Plasma instabilities such as hard disruptions, ELMs, and VDEs will cause both surface and bulk damage to plasma-facing and structural materials. Surface damage includes high erosion losses attributable to surface vaporization, spallation, and melt-layer erosion. Bulk damage includes large temperature increases in structural materials and at the interfaces between surface coatings and structural materials. These large temperature increases can cause high thermal stresses, possible melting and detachment of surface material, and material fatigue and failure. Other bulk effects of plasma instabilities, particularly those of longer duration, such as VDEs, and those with deeper deposited energy, such as runaway electrons, can deliver high heat flux values at the coolant channels, possibly causing burnout of these tubes [2]. In addition to these effects, the transport and redeposition of the eroded surface materials to various locations on plasma-facing and nearby components are a major concern for plasma contamination, safety (dust inventory hazard), and successful and prolonged plasma operation after instability events [3], Fig. 1 is a schematic illustration of the various interaction zones and physics currently included in the High Energy Interaction with General Heterogeneous Target Systems (HEIGHTS) simulation package in a self-consistent and integrated way during plasma instability events.

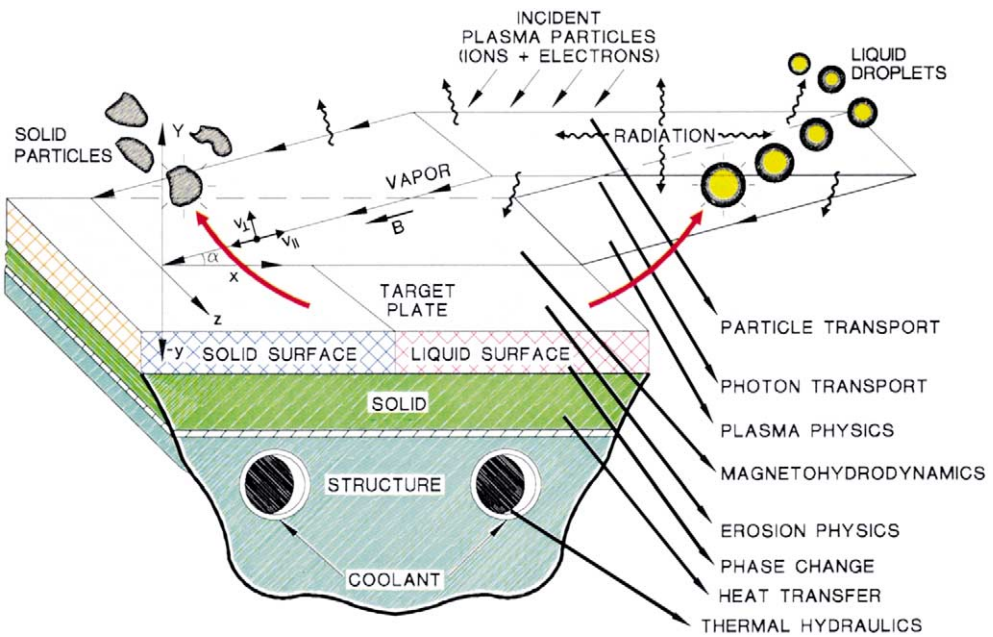

Fig. 1. Schematic illustration of various interaction zones and physics involved during plasma instabilities.

Several key factors can significantly influence the overall response and erosion lifetime of a PFC as a result of the intense energy that is deposited during these plasma instabilities. These factors are, (a) characteristics of particle-energy flow (i.e. particle type, kinetic energy, energy content, deposition time, and location) from the scrape-off-layer (SOL) to the divertor plate; (b) characteristics of the vapor cloud that develops from the initial phase of energy deposition on target materials and its turbulent hydrodynamics; (c) photon-generated continuum and atomic line radiation and transport in the vapor cloud and nearby regions; and (d) characteristics of plasma–solid-melt-layer–debris interactions.

The HEIGHTS simulation package has been developed to study in detail the various effects of sudden high-energy deposition of various sources on target materials [4]. The package consists of many integrated models that follow the beginning of a plasma disruption at the SOL up to the transport of the eroded debris and splashed target materials as a result of the deposited energy. One model in the package, the SOLAS code, describes the plasma behavior in the SOL during a disruption and predicts the plasma parameters and conditions at the divertor plate [5].

To evaluate the various damage mechanisms to plasma-facing and nearby components caused by plasma instabilities, we have developed full multidimensional comprehensive radiation magnetohydrodynamic (MHD) models that use advanced numerical techniques such as particle-in-cell (PIC), forward-reverse, and Ray Tracing methods [4]. These models, which use such advanced numerical methods, are needed for a realistic analysis of disruption conditions and overall consequences. Detailed physical models of plasma–solid–liquid–vapor interaction in a strong oblique magnetic field have also been developed in a fully self-consistent multidimensional model that is coupled with radiation MHD models.

Factors that influence the lifetime of PFCs such as loss of vapor-cloud confinement and vapor removal due to MHD instabilities, damage to nearby components from intense vapor radiation, melt splashing, and brittle destruction–explosive erosion of target materials, can also be modeled in detail [6,7]. The HEIGHTS package being used for reactor design estimates is validated against well-diagnosed experiments in disruption simulation facilities [8]. A major part of the current work focuses on modeling the behavior and erosion of a metallic surface with a liquid layer, subject to various internal and external forces during the energy deposition phase, as on the explosive erosion, and on the characteristics of brittle-destruction erosion associated with carbon-based materials (CBMs). Although in general, good agreement is found for many of the cases studied, discrepancies still exist and must to be resolved.

Accurate prediction of mass losses requires full descriptions of evolving media above the target surface that consist of a mixture of vapor and macroscopic particles (MPs) moving toward the disrupting plasma as schematically illustrated in Fig. 1. Photon radiation from the upper hot region of the vapor will then be absorbed by both divertor surface and the surface of the ejected MPs. This leads to further surface vaporization of divertor and MP surfaces. In such a mixture, additional screening of the target surface by the MP cloud can occur. This could lead to a significantly reduced power flux to the surface due to 'droplet shielding', which is analogous to the vapor shielding effect [3]. In a well-confined vapor cloud, the flight lifetime of MPs in the vapor is short, and complete burning of the emitted MPs occurs. This droplet shielding effect can lead to further reduction of the total erosion loss.

To correctly predict macroscopic erosion, a four-moving-boundaries problem is solved in HEIGHTS [4]. The front of the vapor cloud is one moving boundary, determined by solving vapor hydrodynamic equations. The second moving boundary, due to surface vaporization of the target, is calculated from target thermodynamics. A third moving boundary, behind the surface vaporization front, is due to the melt-splashing front. Finally, the fourth moving boundary is at the liquid–solid interface; it further determines the new thickness of the melt layer. The SPLASH code (part of the HEIGHTS package) calculates the macroscopic mass losses by using the splashing-wave concept as a result of each macroscopic

erosion-causing mechanism [4]. Thus, total erosion is calculated from the sum of all possible erosion mechanisms. An overall assessment of erosion lifetime of PFCs should then include atomic surface vaporization, macroscopic erosion from liquid–metal splashing and brittle destruction of CBMs, and erosion damage to nearby components from intense vapor radiation and deposition.

2. Plasma–material interaction leading to melting and vaporization

Plasma-facing surfaces are rapidly heated during plasma instabilities by direct impact of energetic plasma particles and radiation. The energy deposition in the bulk material is calculated by using models that include the physics of energy loss by plasma ions and electrons in target materials. HEIGHTS package calculates in detail the spatial and time dependence of beam energy deposition in various target materials. Energy deposition methods include analytical, semi-empirical, and Monte Carlo techniques for accurate prediction of the deposited energy. The deposited energy flux can be high enough to rapidly melt and vaporize the surface material. The thermal response of the material is calculated by solving a multidimensional (up to 3-D) time-dependent heat-conduction equation, with moving boundaries, i.e. the receding eroded surface and the solid–liquid interface, with boundary conditions that include heats of melting and vaporization [2], Most of the calculations presented in this study is, however, is 2-D time-dependent analysis.

It is known that during the early stage of an intense power deposition on a target material, a vapor cloud from the target debris will form above the bombarded surface. This shielding vapor layer, if well confined, will significantly reduce the net energy flux to the originally exposed target surface to only a few percent of its initial incident value; thereby substantially reducing the net vaporization rate [2,9]. Depending on the type of application, this shielding layer can be either beneficial (i.e. the protection is desirable) or harmful (protection is not desirable). For example, the shielding by the earth's atmosphere at the surface of colliding asteroids and comets during entrance can prolong the object lifetime and be more dangerous to earth. Also in laser or electron beam welding or cutting of materials the developed vapor cloud is harmful since it reduces the beam power flux to target surface and, therefore, reducing welding or cutting efficiency. The shielding efficiency of this vapor-plasma cloud will, however, depend on several factors. The net power flux that reaches the target surface determines the net erosion and thus the lifetime of PFCs. Net erosion damage to PFCs due to plasma instabilities should include surface vaporization loss, erosion damage to nearby components from intense vapor radiation, and macroscopic erosion from liquid–metal splashing and brittle destruction of CBMs.

Initially, the neutral vapor emitted from the solid or liquid target surface expands freely across magnetic field lines in the direction normal to the surface. As the cold vapor is heated by incident plasma particles, it becomes ionized and expands, following the direction of the oblique magnetic field lines. The parameters and the dynamics of the target plasma depend on the energy flux and the type of target material. Low-Z target plasma (e.g. carbon, beryllium, lithium, etc.) expands to larger distances from the surface, whereas vapor shields formed from higher-Z materials (e.g. tungsten, molybdenum, etc.) stay closer to the surface. The incoming plasma particles are completely stopped in the vapor plasma and the plasma energy flux is converted to photon radiation. Although reduced from its original value, the net energy flux to the target surface (dominated by photon radiation) is large enough to cause melting and further erosion of metallic components.

The expansion of vapor plasma into the vacuum (surrounding gas or plasma) above the exposed target surface under the influence of a strong magnetic field is determined by solving the MHD equations for conversation of mass, momentum, and energy:

$$\frac{\partial \rho}{\partial t} + \nabla(\rho \vec{V}) = 0, \tag{1}$$

$$\rho \frac{\partial \vec{V}}{\partial t} + \nabla P = \vec{F}, \tag{2}$$

and

$$\frac{\partial E}{\partial t} + \nabla(E\vec{V}) + P\nabla\vec{V} = \nabla(K\nabla T)\nabla Q_r + \nabla Q_b + \frac{\vec{J}^2}{\sigma}, \tag{3}$$

where V is vapor plasma velocity, ρ is density, E is energy, P is pressure, F is external force, K is vapor plasma thermal conductivity, T is vapor temperature, Q_r is radiation flux, Q_b is the incident particle flux from the disrupting plasma, J is plasma current density, and σ plasma electrical conductivity. All variables of these equations are both time- and space-dependent. The plasma beam particle flux deposited in the vapor is calculated by similar methods for the slowing down in cold target i.e. by inelastic and elastic collisions, however, an additional stopping mechanism is used which arises from the free electron due to ionization. This free electron stopping term can substantially shorten the range of both plasma ions and electrons in the ionized vapor leading to high-energy deposition rate at the front vapor zone.

The vapor plasma once ionized and with large electrical conductivity, is assumed to move freely along magnetic field lines. The vapor plasma equation-of-motion is solved in two directions, along and perpendicular to divertor surface. The equation of motion in a strong magnetic field can then be written as:

$$\rho \frac{d\vec{V}}{dt} = -\nabla P + \vec{F}_m, \tag{4}$$

$$\vec{F}_m = \frac{1}{c}[\vec{J} \times \vec{B}], \tag{5}$$

where F_m is magnetic force, J is plasma current density, c is speed of light, and B is magnetic flux density. The induced magnetic force will act as a retarding force to vapor expansion. The electric, ε, and magnetic field B are defined from Maxwell equations:

$$\frac{1}{c}\frac{\partial \vec{\varepsilon}}{\partial t} = \nabla \times \vec{B} + \frac{4\pi}{c}\vec{J} \tag{6}$$

$$\frac{1}{c}\frac{\partial \vec{B}}{\partial t} = -\nabla \times \vec{\varepsilon} \tag{7}$$

The time variation of the induced electric field in the vapor plasma is usually very small. Therefore:

$$\nabla \times \vec{B} = -\frac{4\pi}{c}\vec{J}, \tag{8}$$

and

$$\vec{\varepsilon} = \frac{1}{c}[\vec{V} \times \vec{B}] + \frac{\vec{J}}{\sigma} \tag{9}$$

The time-varying magnetic field in the vapor plasma can then be given by:

$$\frac{\partial \vec{B}}{\partial t} = -\nabla \times [\vec{V} \times \vec{B}] + \nabla \times \left[\frac{c^2}{4\pi\sigma}\nabla \times \vec{B}\right] \tag{10}$$

The magnetic force F_m, is composed of a magnetic pressure force, F_p, and a tension, F_t, due to the curvature of the magnetic field lines, where:

$$F_p = -\nabla\left(\frac{\vec{B}^2}{8\pi}\right) \tag{11}$$

$$F_t = -\frac{1}{4\pi}(\vec{B}\nabla)\vec{B} \tag{12}$$

The melt layer, developed during a disruption, is exposed to various forces, such as electromagnetism, gravitation, mechanical vibration, plasma momentum, surface tension, and ablation recoil [10], For metallic components such as beryllium and tungsten, erosion lifetime due to these abnormal events will be controlled and dominated by the evolution and hydrodynamics of the melt layer during disruption, and the resultant loss of liquid material from the surface. In contrast, CBMs do not melt and, therefore, do not erode by these processes; this was a major reason for the choice of graphite and carbon-fibre-composites for some PFCs in current fusion machines and in the international thermonuclear experimental reactor (ITER) design. However, CBMs may suffer from another splashing erosion mechanism; an explosive-type erosion, as described later.

In future tokamak devices, ≈ 10–200 MJ m^{-2} will be deposited on the divertor plates during the disruption thermal quench, a time of the order of 0.1–10 ms. These corresponds to a heat fluxes

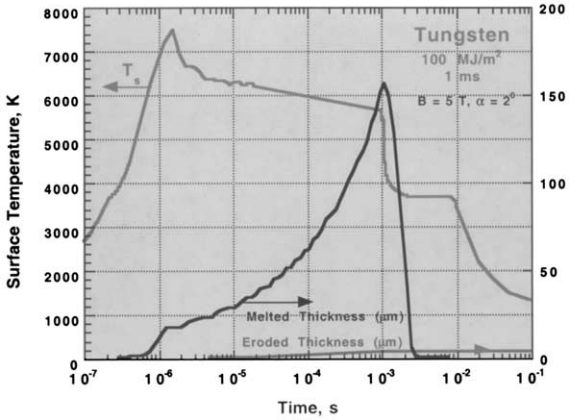

Fig. 2. Time evolution of tungsten surface temperature, melting thickness, and vaporization losses during a disruption.

>10 G m^{-2}. Fig. 2 shows a typical time evolution of a tungsten surface temperature > melt-layer thickness, and vaporization losses during a disruption for an incident plasma energy of 100 MJ m^{-2} deposited in 1 ms, as predicted by the HEIGHTS package [4]. An initial magnetic field strength of 5 T with an incident angle of 2–6° is used in these calculations. The sharp initial rise in surface temperature is due to the direct energy deposition of incident plasma particles at the material's surface.

The subsequent decrease in the surface temperature was caused by the reduction in absorbed heat flux due to vapor shielding and conduction of heat into the material. The subsequent behavior is mainly determined by the energy flux from the emitted photon radiation in the vapor cloud, as discussed above, and by vapor-electron heat conduction.

Fig. 3 shows tungsten solid–liquid–vapor temperatures as a function of distance for 10 MJ m^{-2} energy density deposited at two disruption times, i.e. 0.1 and 1 ms. At the shorter disruption time, both the liquid–solid and the vapor temperatures are higher than in the case of longer disruption times. A longer disruption time causes the vapor to expand to larger distances above the divertor surface and also causes the energy flux that reaches the divertor surface to diffuse deeper into the bulk and produce a thicker melt layer. An order-of-magnitude increase in the energy density, i.e. from 10 to 100 MJ m^{-2} would only result in about 30% increase in the erosion rate and less than that in melting thickness. This is mainly because most of the incident plasma energy is used to heat up the front regions of plasma vapor [6]. This means that most of the radiation-flux is emitted in the direction away from the PFCs. Depending on the divertor design and configura-

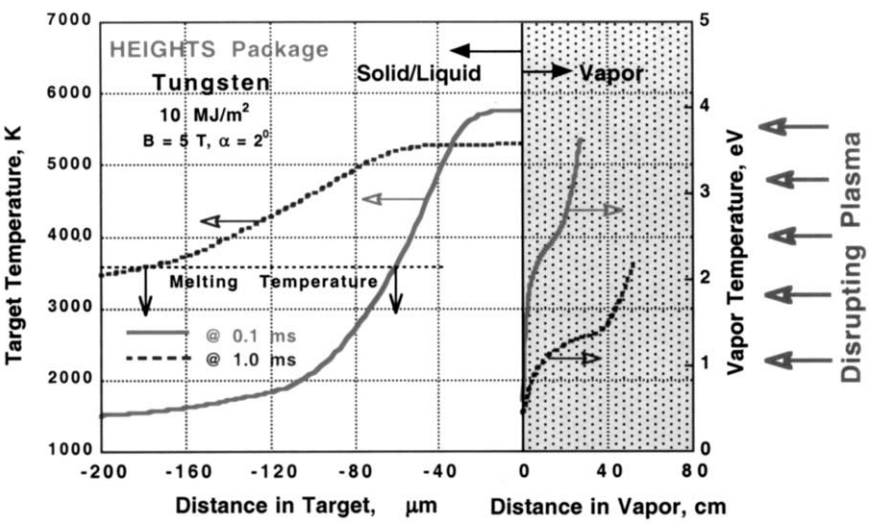

Fig. 3. Spatial evolution of tungsten solid–liquid–vapor cloud temperatures at two disruption times.

tion, the expanding hot vapor and its radiation can damage nearby components, particularly for closed-divertor configurations. It is, therefore, desirable to keep the normal expansion of vapor to a minimum.

Based on the above results, for a disruption energy density of ≈ 10 MJ m^{-2} and a disruption time of 1 ms, the calculated vaporization and melting thickness for a tungsten plate are about 2 and 180 μm, respectively. The vaporized 2 μm thick layer expands 30–60 cm in vapor cloud above the target surface. The melt layer thickness is much more than the vaporized thickness, therefore, the lifetime of a metallic target would strongly depend on the fraction of melt layer lost per event. A sacrificial 20-mm-thick carbon layer would then lead to a lifetime of > 500 disruptions due to vaporization alone (i.e. without including erosion from other mechanisms, as will be discussed later) or a lifetime of 130 disruptions for tungsten if 50% of the melt layer is lost for the above disruption energy density and duration. It has also been found that, depending on the divertor configuration and design, the transport and deposition of the radiation generated from the primary vapor cloud can be high enough to cause severe melting and erosion of nearby components. The vapor cloud that develops on the front of the surface of the nearby components may not be as effective as the primary cloud in protecting adjacent components because of strong vapor diffusion losses, vapor-cloud optical properties, and geometrical effects [11].

The detailed vapor motion above the exposed surface and its stability–confinement is calculated by solving the vapor MHD equations in two dimensions for conservation of mass, momentum, and energy under the influence of a magnetic field [12,13]. The vapor cloud, if well confined, greatly reduces the net energy flux to the surface, leading to one to two orders of magnitude less erosion by vaporization [9], The magnetic field lines are initially frozen into the surface of the liquid metal layer because of the liquid's high conductivity. However, as more vapor is emitted from the surface, the expanding dense ionized vapor will sweep and distort the oblique magnetic field lines. Near the upper vapor boundary, the magnetic field lines become almost parallel to the vapor surface. Such a situation of distorted magnetic field distribution leads to a flute-type MHD instability in the vapor plasma [13], As a consequence of the loss of vapor confinement, the turbulent diffusing hot vapor may then deposit its energy on nearby components, causing more erosion. The overall net erosion rate and resultant damage will depend on the parameters of the disrupting plasma, the size of the disruption spot, design configuration, and the type of PFM. In addition, the incidence of the hot disrupting plasma onto the cold plasma of the vapor shield may give rise to electric fields [14]. The electric field may cause lateral $\vec{E} \times \vec{B}$ drifts that can lead to deflection of either the vapor shield plasma [15] or the incident plasma [16], or both. Experimental evidence for the influence of $\vec{E} \times \vec{B}$ drifts on plasma shield efficiency and erosion is not yet proved.

Photon radiation and transport in the vapor plasma are very important in predicting disruption erosion of PFCs. Opacity and emissivity data for the developed vapor plasma varies significantly because the vapor contains very cold and dense plasma regions near the target surface and very hot and less-dense plasma regions where the disrupting plasma ions and electrons deposit their energy. The models in the HEIGHTS package [2] allow for the treatment of nonlocal thermodynamic equilibrium (non-LTE) of the vapor-cloud-generated plasma, multigroup and multidimensional analysis of the produced photon spectra, and self-consistent kinetic models for both the continuum and line radiation generated in the vapor cloud. Calculated photon spectra emitted from the outermost regions of tungsten vapor for two deposited plasma energy densities (10, 100 MJ m^{-2}) and for beryllium at 100 MJ m^{-2} are shown in Fig. 4. Most of the incident plasma energy flux ($> 80\%$) during the disruption is quickly converted into radiation energy in the vaporized material. Most of the radiation energy will be deposited at locations other than the original disruption location. In some cases, the damage from the plasma-energy-converted radiation can exceed the damage at the original location, particularly in a closed divertor configuration.

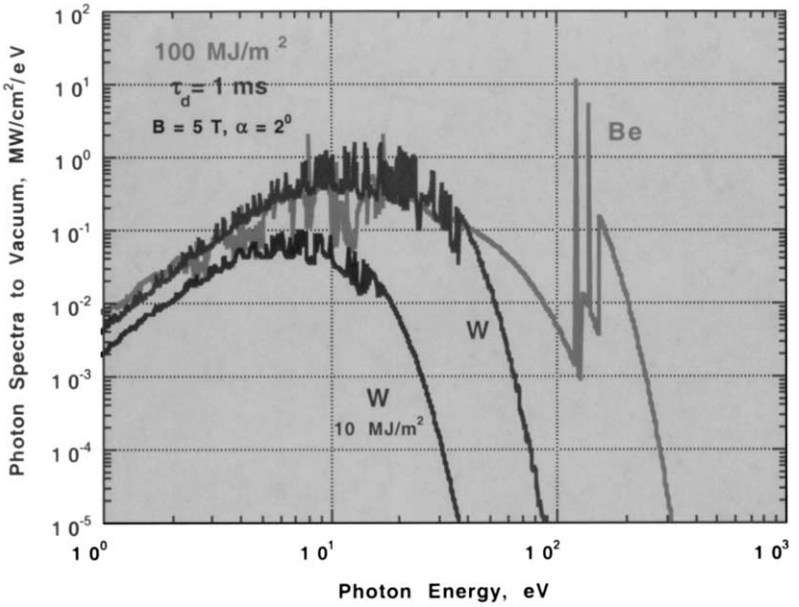

Fig. 4. HEIGHTS—calculated photon spectra emitted from outermost vapor regions for different deposited plasma energies.

The emitted radiation spectrum depends on vapor–plasma parameters such as vapor temperature and vapor density, which is determined from the detailed physics of vapor–plasma interactions. For the case of higher energy disruption, more power is deposited in the vapor that heats the vapor front to higher temperatures and causes it to emit harder photon spectra, which in turn, deposit more energy at the material surface. Due to its lower atomic number, beryllium vapor is much less radiant than the higher-atomic-number tungsten vapor; therefore, its temperature is much higher than that of tungsten vapor and consequently, its photon spectrum is harder and the yield is much higher.

Line radiation in the vapor is particularly important for materials with lower atomic numbers and high-temperature vapor clouds. In many cases of disruption on beryllium targets, $>90\%$ of the emitted radiation energy is in the form of a few strong lines of radiation. Careful treatment of line transport in vapor clouds is important and required to correctly calculate the net energy flux to the material surface [2].

3. Material erosion mechanisms

3.1. Erosion in metals including macroscopic particle formation

Surface vaporization losses of metallic PFMs are generally small (only a few μm) over a wide range of plasma conditions during short plasma instabilities [2]. In most disruption cases, the melt-layer thickness of metallic components can be one to two orders of magnitude higher than surface vaporization losses [3], as shown in Fig. 2. The loss of melt layer during the course of a disruption will seriously decrease the erosion lifetime of PFCs. During a reactor disruption, the melt layer is subject to various forces such as electromagnetism, gravitation, mechanical vibration, plasma momentum, surface tension, and ablation recoil. Several mechanisms can cause melt-layer loss during plasma instabilities [10]. Experimental observations in laboratory disruption simulation devices are, however, consistent with two important mechanisms of melt-layer removal [1]. These mechanisms are melt splashing due to the formation, growth, and explosion of vapor bubbles

inside the liquid layer, and growth of hydrodynamic instabilities due to plasma impact momentum ('plasma wind') at the liquid surface and forces generated by current decay in the liquid metal layer.

Therefore, hydrodynamic instabilities, such as the Kelvin–Helmholtz (K–H) instability, will arise and form liquid droplets that will be carried away by the plasma wind. The amount and rate of melt-layer loss is difficult to predict and is expected to depend on many parameters, such as heat flux, impurity and gas content, material properties, and disrupting plasma parameters. More work is needed to study the details of macroscopic erosion of metallic materials during an intense deposition of energy.

3.2. Erosion in carbon-based materials

Due to the self-shielding layer effect discussed above, erosion by vaporization of carbon materials is also limited to < 10 μm for a wide range of disrupting plasma conditions. This is about only one to two orders of magnitude lower than it would be if no vapor shielding exist [9]. However, in many cases, graphite and CBMs have also shown large erosion losses that significantly exceed losses from surface vaporization. A phenomenon, called 'brittle destruction', has been observed in various disruption simulation facilities [4], Physical mechanisms that cause brittle destruction of CBMs are not yet clear. One mechanism could be cracking caused by thermomechanical stresses that develop during the intense deposition of energy [17–19], Another proposed mechanism is that material is ejected by the sharp rise in the pressure of gas trapped in the network of pores between intergranular and intercrystallite boundaries that can cause explosive ejection of material [20]. These processes are likely to depend on the material microstructure.

The macroscopic erosion of CBMs will depend on three main parameters, net power flux to the surface; exposure time; and the threshold energy required for brittle destruction [20]. The required energy is critical in determining the net erosion rate of CBMs and is currently estimated from disruption simulation experiments. More experimental data and additional detailed modeling are needed to evaluate the erosion of CBMs, e.g. the role of brittle destruction.

Surface ablation, i.e. formation and ejection of MPs, is characterized by splashing or destruction waves, assuming that a layer of material heated above certain threshold energy is removed in the form of MPs [7]. Ablation of both melting and carbon-based materials is occurs in splashing–destruction waves when a layer of material is heated above a certain threshold energy, Q_{th}, and is removed in the form of MPs, This energy threshold for splashing is roughly equal to the sum of a thermal energy Q_{heat} (required to heat the liquid above a certain threshold temperature T_{th} including heat of fusion, Q_f, for melting materials), a separation energy to remove the MPs from the surface, and a kinetic energy for the moving droplets. The separation energy of the splashed droplets is determined from the surface tension of the liquid metal. The value of Q_{th} is, therefore, calculated from:

$$Q_{th} = Q_{heat} + Q_s + Q_k, \tag{13}$$

where:

$$Q_{heat} = \int_{T_o}^{T_{th}} c_v \mathrm{d}T + Q_f \quad \text{(for melting materials)} \tag{14}$$

$$Q_s = N_{drop} 4\pi R_{do}^2 \sigma_s, \quad N_{drop} = \frac{\mathrm{d}m/\mathrm{d}t}{V_{do}(4/3)\pi R_{do}^3}, \tag{15}$$

and,

$$Q_k = \frac{1}{2}\rho V_{do}^2 \tag{16}$$

where T_o is initial material temperature, c_v is specific heat, Q_s is energy required for droplets separation, Q_k is kinetic energy of ejected MP, V_{do} is ejected velocity, R_{do} is radius (size), N_{drop} is density of the ejected MP, $\mathrm{d}m/\mathrm{d}t$ is ablation rate, and as is surface tension. For hydrodynamic instabilities, T_{th} is near the melting temperature T_{melt}, while for bubble boiling, T_{th} is near the vaporization temperature T_{vap}. Therefore, the threshold energy for macroscopic erosion is determined from material properties, mechanism of macroscopic destruction, and dynamics of vapor-cloud expansion above the target surface.

Macroscopic brittle erosion of CBMs from thermal stresses and macroscopic pore explosion can be described in a way similar to that used for metallic materials, by using the concept of a destruction wave, with the separation energy Q_s, defined in this case from the binding energy of the grains–crystallites. Since the MPs are ejected as a result of the vapor pressure P, similar to the external pressure P_{out}, the velocity of MPs can be estimated from $V_{do} \leq \sqrt{P_{out}/\rho}$. For a P_{out} of ≈ 50 atm (pressure of vapor cloud), $V_{do} \approx 50$ m s^{-1} [7].

4. Interaction between macroscopic particles and vapor plasma

The ejected waves of MPs will form a 'droplet cloud' above the target surface and expand inside the initial vapor cloud. MPs are treated as separate media that interact with the surrounding inhomogeneous vapor-cloud plasma through exchange of mass, momentum, and energy. To calculate of mass and energy exchange, MP vaporization is calculated by equations similar to those for vapor-cloud dynamics [7]. Mass losses and the corresponding decrease in MP radius (size) are calculated by solving the mass, momentum, and energy conservation equations given by [21]:

$$\frac{dR_d}{dt} = -\frac{\varphi_{out}}{N_{drop}}, \tag{17}$$

$$\frac{dE_d}{dt} = W_{rad} + W_{cond} - 4\pi R_d^2 \varphi_{out}(c_v T_d + Q_f + Q_v) \tag{18}$$

where E_d is net energy of MP, W_{rad} and W_{cond} are radiation and conduction energy fluxes, φ_{out} is net vapor flux from MPs surface, T_d is surface temperature of MP, and Q_v is heat of vaporization. The net vapor flux from the MPs surface is defined as the difference between the vapor flux leaving the surface (corresponding to the surface temperature) and the vapor flux from the surrounding vapor cloud that condenses at the MPs surface. Due to the decreasing MP radius, the interaction of MPs with vapor can be either collisional or collisionless. The collisionality condition is determined by the parameter, ζ, where:

$$\zeta = \frac{1}{6}\left(\frac{V_o}{V_d}\right)\left(\frac{R_d}{\lambda_o}\right), \tag{19}$$

where the subscript o refers to the vapor media and λ_o is vapor mean free path. For $\zeta > 1$, the Stokes formula with viscosity ηd is used while for $\zeta \leq 1$, the friction force is calculated assuming the interaction of freely moving vapor with spherical particles. Absorption of photon radiation power by each MP is calculated by using the absorption cross section that takes into effect geometrical screening by other MPs. The total absorption and reflection of photon radiation are summed over all emitted MPs. Influence of a magnetic field on MPs motion and dynamics is negligible, therefore the $[J \times B]$ force is not taken into account. Fig. 5 is a schematic illustration of MP evolution and interaction with the vapor cloud during a plasma instability event.

Once MPs are emitted into the vapor plasma, they will alter the hydrodynamic evolution of the vapor plasma. The corresponding coupled mass-, momentum-, and energy-conservation equations become complicated and are given simply in conventional terms by [21]:

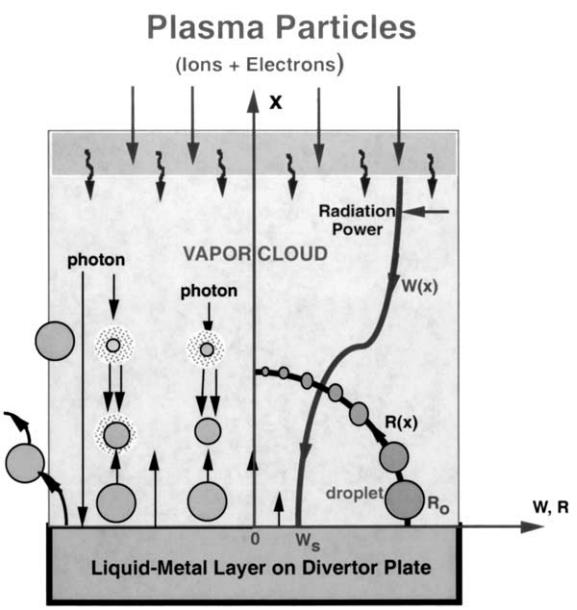

Fig. 5. Schematic illustration of droplet shielding concept during plasma instabilities.

$$\frac{\partial \rho}{\partial t} + \nabla(\rho \vec{V}) = \nabla \vec{S}_{\text{net}}, \tag{20}$$

$$\rho \frac{\mathrm{d}\vec{V}}{\mathrm{d}t} = -\vec{\nabla} P + \frac{1}{c}[(\nabla \times \vec{B}) \times \vec{B}] + \vec{F}_{\text{plas}} + \vec{F}_{\text{MP}}, \tag{21}$$

$$\frac{\mathrm{d}E}{\mathrm{d}t} - \frac{E}{\rho}\frac{\mathrm{d}\rho}{\mathrm{d}t} + P\nabla \vec{V} = -\nabla \vec{q}_{\text{k}} + Q_{\text{plas}} + Q_{\text{MP}} + Q_{\text{rad}} + \nabla \vec{W}_{\text{net}}, \tag{22}$$

where S_{net} is net vapor flux from droplets surface, F_{plas} is deposited plasma momentum, F_{MP} is deposited droplet momentum in the vapor-cloud, q_{k} is heat conduction flux along and across the magnetic field, Q_{plas} is SOL plasma energy flow to the vapor cloud, Q_{MP} is droplet kinetic energy in the vapor, Q_{rad} is radiation power, and W_{net} is energy flux from vaporizing droplets. The vapor energy density, E, consists of both the thermal and ionization energy:

$$E = \frac{3}{2}(1+z)nkT + n\int_{o}^{z} I(z)\mathrm{d}z, \tag{23}$$

where n is vapor number density and $I(z)$ is the ionization potential of the vapor plasma.

One purpose of this work is to study vapor plasma dynamics in a mixture of atomic vapor and MPs in order to find the contribution of ablation losses relative to total mass losses. If the vapor plasma is well confined by the magnetic field, there is no motion of the vapor plasma along the divertor surface in the poloidal direction, (φ, and MP dynamics are determined by their interaction with the vapor plasma moving in both toroidal, φ, and radial, r, directions. Therefore, MPs remain within the vapor cloud up to full vaporization, i.e. complete burning or until leaving the vapor cloud in the r direction.

Photon radiation transport inside the vapor plasma will finally determine net energy flux to the surface and consequently will determine the lifetime of the target plate. For quasi-stationary conditions, the transport equation for the radiation has the form:

$$\vec{\Omega}\nabla \vec{I}_{\nu} = \varepsilon_{\nu}\vec{I}_{\text{vp}} - \chi_{\nu}\vec{I}_{\nu} \tag{24}$$

where $\vec{I}_{\nu}$ is the radiation intensity, $\vec{I}_{\text{vp}}$ is the Planckian radiation, ν is the frequency, ε_{ν} is the vapor plasma emission coefficient, Ω is the solid angle, and χ_{ν} is the vapor and MPs absorption coefficient The 'forward–reverse' method is used in this analysis to calculate the photon radiation transport in the vapor–droplet plasma. The corresponding equations in two directions are given by [21]

$$\pm\frac{1}{2}\frac{\mathrm{d}I_{\nu}^{\pm}}{\mathrm{d}x} = \varepsilon_{\nu}I_{\text{vp}}^{\pm} - \chi_{\nu}I_{\nu}^{\pm} \tag{25}$$

$$W_{\text{rad}}^{\pm} = \int_{0}^{\infty} I_{\nu}^{\pm}\,\mathrm{d}\nu, \quad W_{\text{rad}} = W_{\text{rad}}^{+} + W_{\text{rad}}^{-} \tag{26}$$

where I_{ν}^{+} is the photon flux moving upward (forward), I_{ν}^{-} is the photon flux moving downward (reverse), and W_{rad} is the total emitted radiation. To calculate ε_{ν} and χ_{ν}, as well as thermodynamic properties, full kinetic equations are solved in the evolving vapor-cloud plasma for all level populations of charged particles. The kinetic equations are solved at each time step, taking into account induced radiation; therefore, radiation transport were calculated in a self-consistent way. In these calculations, the radiation flux is composed of two separate components, continuum radiation flux and line radiation flux. The continuum spectrum is divided into multigroups in logarithmic scale for a wide range of photon energy. The radiation transport for each line is calculated separately, also using multigroup approximation for each line. For most cases, the number of groups for the continuum spectra $N_{\text{c}} > 1000$ and for lines $50 \leq N_{\text{L}} \leq 500$ depending on target vapor material and condition. Therefore, radiation transport in the vapor plasma was calculated for a total number of groups that exceed several thousand.

The front hot and less-dense vapor cloud expands in the normal direction with a vapor cloud velocity of ≈ 1 km s^{-1}. However, the front vapor plasma does not influence the denser and colder vapor near the target surface that contains the MPs. The effective size of this front part of the vapor cloud is determined by absorption depth of the incoming plasma particles, particularly plasma electrons. After a transition time of a few tens of μs, depending on target material, the spatial distribution of plasma parameters (such as density, temperature, and magnetic field) become quasi-stationary, as shown for a beryllium target (at 400

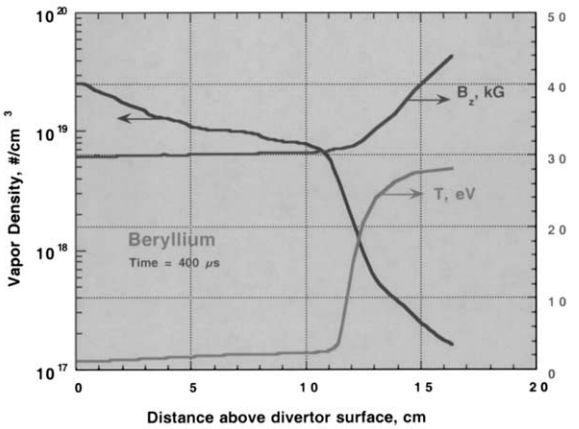

Fig. 6. Spatial evolution of beryllium vapor temperature, density, and toroidal magnetic field during a disruption.

μs snapshot) in Fig. 6 [21]. At the front of the expanding vapor cloud, density is lowest ($n \approx 2 \times 10^{17}$ cm^{-3}) and temperature is highest ($T \approx 28$ eV). The denser and colder vapor region actually consists of two zones. The first zone, very near the target surface, is governed by MP vaporization, thus, density is high and temperature is low ($T \approx 0.3$–0.5 eV), which means that the vapor is mostly neutral ($Z < 0.5$) in this zone. The second zone consists of vapor plasma with $Z \approx 1$ and is characterized by a low or negligible radiation. The little radiation absorbed by some free electrons is enough to keep the vapor at this temperature. Most of this radiation S_{in}, is absorbed by MPs near the target surface. Flowing vapor from the target surface pushes upward on the magnetic field, therefore, the field in the vapor cloud is decreased to $B_z \approx 3$ T in beryllium vapor. Thus, the inclination angle of the magnetic field lines in the vapor cloud changes from $\alpha_o = 6°$ to $\alpha \approx 20°$.

Fig. 7 shows the spatial distribution of deposited plasma power (S_{plasma}), upward radiation flux (S_{out}) and downward radiation flux (S_{in}) toward the target [21]. The energy of plasma particles is absorbed mainly by the free electrons of the vapor at high temperature and high Z and by the inner shell electrons at lower Z. It can be seen that the upward radiation is generated in this region. However, the radiation power toward the target surface S_{in} is absorbed mainly by vapor plasma with lower $Z \approx 1$. For lithium, the size of the radiative region is similar to the size of the zone where incoming plasma flux is absorbed. For higher-Z materials such as beryllium and carbon, the radiation heat conduction is high enough to keep part of the vapor plasma outside the absorption zone at a higher temperature. Radiation absorption ceases at temperatures lower than the ionization temperature. Near the wall, the second zone of the cold region contains MPs that can absorb radiation; thus, a sharp decrease occurs in S_{in} as shown in Fig. 7.

The ejected MPs move across the cold dense vapor with a maximum velocity at ejection $V_{ej} < 100$ m s^{-1}, determined from the vapor pressure above the target surface. Nevertheless, the MPs are slowed down because the vapor velocity near the target surface is $< V_{ej}$. Fig. 8 shows the spatial evolution of a lithium droplet with an initial radius of 10 μm and velocity of 50 m s^{-1} as it moves across the lithium vapor cloud at time = 400 μs. The lithium droplet is completely vaporized at a distance < 2 mm above the target with a lifetime τ_{life} of ≈ 40 μs in the vapor cloud. The 'birth time', i.e. time when the particle–droplet was ejected, is also shown. The MPs that were born earlier were moved a far distance from the target surface for a longer time. A beryllium droplet travels much longer distance than a lithium droplet because of its higher vaporization energy and less radiation power to the droplet

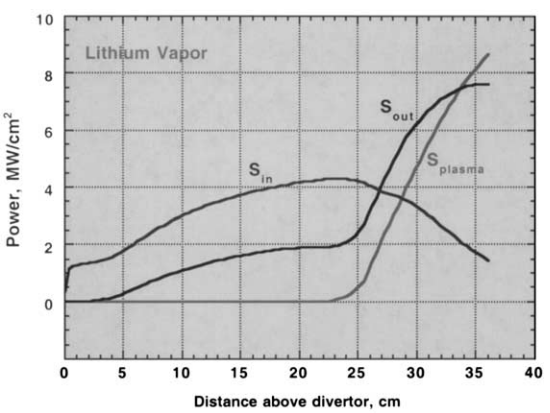

Fig. 7. Spatial distribution of emitted radiation and deposited plasma power in Li vapor.

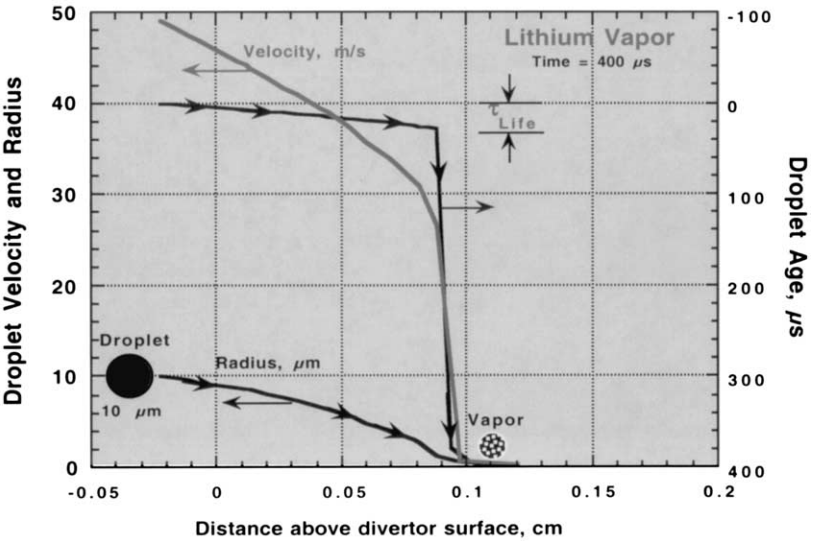

Fig. 8. Spatial evolution and lifetime of a lithium droplet as it moves in vapor cloud.

surface (S_{tgt}[Be] ≈ 230 kW cm^{-2} vs. S_{tgt}(Li) ≈ 300 kW cm^{-2}). The lifetime of MPs is determined by the incoming radiation power and vaporization energy; thus, τ_{life}(Li) ≈ 40 μs, but τ_{life}(Be) ≈ 240 μs, and τ_{life}(C) > 400 μs [21].

The mechanism and dynamics of a splashing–destruction wave can be described as follows. During the initial phase, the target surface is heated by both plasma particles and photon radiation while the surface temperature is achieving the threshold temperature–energy. Then, a splashing wave propagates into the target bulk. The front wave position x_{wave} inside the target is determined by the threshold condition $T(x_{wave}) = T_{th}$. All of the target mass behind the wave front with $x < x_{wave}$ is emitted in the form of MPs. Depending on material properties and mechanism of splashing–brittle destruction, these MPs exhibit certain distributions in size R_{do}, velocities V_{do}, and angles of ejection. Detail calculations have also shown that the initial distribution of MP size and velocities does not affect the net radiation power to the target surface, only the vaporization path length of the MPs [21].

The process of ablation mass loss can be divided into two stages. During the first stage the splashing wave propagates quickly, because the target surface is heated near T_{th} at a sufficient depth, and any slight additional radiation power is enough to achieve threshold conditions. Therefore, sufficient mass is ejected in a short time; both the mass and time are determined by the material properties. The time evolution of the beryllium target surface temperature T_s and droplet and total vapor mass losses are shown in Fig. 9. The time history of the splashing erosion wave of beryllium droplets is shown. The target surface temperature achieves a quasi-stationary value after a certain time.

During the second stage, after the first ejection wave, the splashing process is quasi-stationary and the flux of newly ejected MPs becomes equal to the flux of the vanishing MPs [2]. For a lithium target, this state is quickly achieved in < 20 μs, but for materials with higher T_{vap} such as beryllium, this state is achieved at the much later time of ≈ 150 μs. For materials with even higher T_{vap}, like CBMs, such a state was not achieved in up to 600 μs. The total mass loss of beryllium targets is only ≈ 10–15% of the total melting thickness for well-confined vapor and droplet clouds.

The total mass loss is, therefore, determined from the net radiation flux that arrives at the target surface after the double shielding effect that is due to absorption by both vapor plasma and MPs. After a certain transition time, these fluxes,

as well as the front vapor cloud temperature achieve the quasi-stationary state. The vapor and droplet shielding efficiency is $>95\%$ for the candidate materials and the conditions studied in this analysis.

5. Results from simulation experiments

Disruption conditions in next-step devices cannot be achieved in existing tokamaks because of the large difference in stored energy in the two devices. Therefore, laboratory experiments (e.g. laser and electron beams, open plasma traps and plasma guns) are used to study and simulate disruption erosion effects [22–26], The results of these experiments are used to validate the above-discussed theories and models, which are currently under development for the purpose of predicting effects in a next-step device.

Laser and high-energy electron beam facilities have been widely used to test divertor materials, primarily graphite and carbon-based materials [25,26]. These experiments, mainly carried out in facilities without a magnetic field (known to confine vapor plasma near the surface of the exposed material samples), and thus in the presence of a poor shielding efficiency, have typically shown very high erosion rates (hundreds of μm). In laser beams, this is due to the fact that the beam size is generally very small (≤ 2–4 mm) and penetrates the expanding cloud of vaporized material with little attenuation. In electron beams, because of the high kinetic energy (100–150 keV), the electrons penetrate the vapor and the target material more than in laser or plasma gun devices. Thus, the vapor cloud is heated to lower temperatures than in plasma gun experiments, and the fraction of incident energy that is dissipated via radiation in the vapor is much lower [13].

Experiments carried out in a particular type of simulator devices, e.g. the GOL-3 facility, which uses a combined hot electron beam (low MeV range) and low-temperature plasmas (≈ 3–5 eV), led to an explosive-type high erosion of graphite materials [27]. Approximately 500 μm per shot of graphite was eroded by an energy density of 30 MJ m^{-2}. The enhanced graphite erosion can be explained in terms of the volumetric energy deposition causing significant bulk damage and the eroded graphite being emitted in the form of grains ranging in size between 1 and 40 μm. The conditions in this facility, however, may not be fully relevant to disruption conditions in toka-

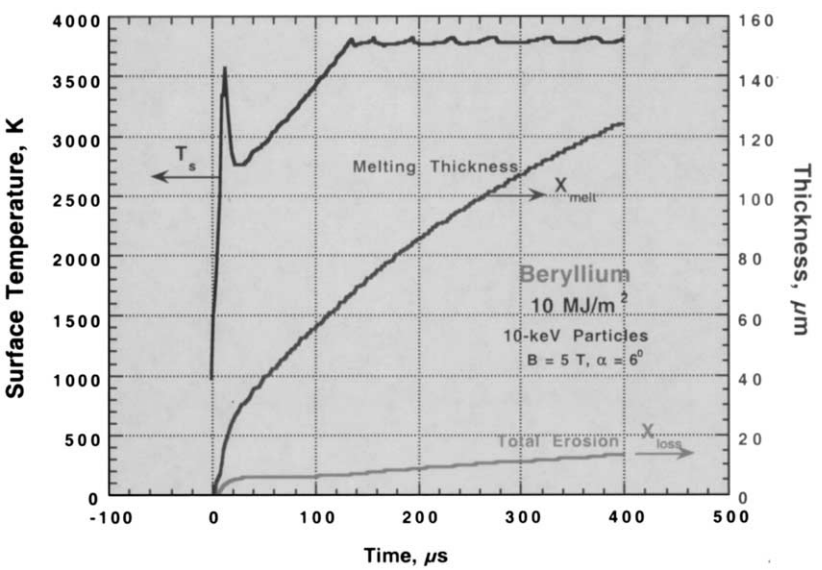

Fig. 9. Time evolution of beryllium target surface temperature, droplet mass, and total vapor mass.

maks because there are no such hot electrons during a tokamak thermal quench disruption.

Plasma gun devices, which typically produce low-temperature plasmas ($T < 1$ keV) and high-energy flux (up to 10–20 MJ m^{-2} deposited in a pulsed duration of < 1 ms), are more suitable than electron or laser beams for simulating relevant reactor disruption conditions. These facilities are primarily used to study the underlying physics of the plasma–surface interactions during disruptions and quantify the resultant material target erosion. One relevant gun-facility is the MK-200UG, which can produce hydrogen and deuterium plasma streams with a total energy of 50 kJ and ion kinetic energy > 1 keV in a magnetic field of 2–3 T [24]. Target materials can be tested at perpendicular as well as in an oblique plasma incidence. The main disadvantage of this facility is its very short pulse duration, i.e. $t \approx 40$–50 μs, which makes it suitable to simulate only the early stages of a disruption in a next-step tokamak. Quasi-stationary plasma guns such as VIKA and QSPA generate plasma streams with sufficiently long-pulse duration [22,23]. However, because of the relatively low kinetic energy of the ions ($E_i =$ 100–300 eV), and large plasma densities ($> 10^{22}$ m^{-3}), a shock wave may arise during plasma deposition and this could lead to a deceleration of the plasma stream and to a 'self-shielding' effect that mitigates the energy flux that reaches the material surface and leads to an underestimation of erosion when compared with actual tokamak conditions.

Several experiments have been performed in various plasma gun facilities, primarily to study physical properties and shielding efficiency of plasma vapor shields and the resultant material erosion. In these experiments, the plasma temperature and density distributions in the vapor shielding layer are measured along with the lateral leakage of radiation by Thomson scattering and optical and soft X-ray interferometry. Material erosion damage is generally measured by surface profilometry and mass loss. Vapor shielding reduces erosion, at least to some extent, in most disruption simulation facilities. The dependence of the density and temperature of plasma vapor on the incoming plasma flow and the target material is generally in good agreement with theory [13]. At perpendicular plasma impact, the target plasma expands upwards toward the plasma stream along the magnetic field lines, and transverse motion is inhibited by the strong magnetic field. At oblique incidence, the vapor shield of carbon material drifted in the direction of the magnetic field lines, along the inclined target surface, and the oblique magnetic field does not totally prevent transverse plasma motion [28]. This mechanism depletes the shielding properties and increases the erosion of a graphite target by $\approx 50\%$. This finding was in agreement with modeling predictions, carried out prior to the experiments, to model the effect of vapor loss due to instabilities [20]. Additional analysis is needed to determine the underlying cause of this drift.

Recent gun experiments have also shown collateral damage of nearby surfaces from radiation emitted from the outermost regions in a well-confined vapor cloud [28]. A graphite erosion of 0.35 μm per shot was caused by radiation emitted from a plasma vapor that formed in front of a tungsten target (≈ 1 MJ m^{-2}). This erosion is similar to that observed for direct plasma impact (0.4 μm per shot) at much higher heat flux (≈ 15 MJ m^{-2}). This finding is in agreement with results of modeling [29], and is attributed to the fact that the shielding efficiency is lower under radiation heat loads than under direct plasma impact. The secondary radiation is, therefore, an important consideration for the choice of divertor materials and geometry in future tokamak devices.

For CBMs, strong erosion with considerable mass losses that exceed those from surface vaporization is also observed in plasma-gun devices. Experiments in the MKT facility have shown emission of MPs [30]. Recently, experiments performed in MK-200UG [31] and QSPA [32] have also revealed macroscopic erosion mechanisms.

Several studies have also been carried out in recent years to investigate the macroscopic erosion of metals under disruption conditions [33]. Preliminary analysis of the microstructure of the exposed metal surfaces has clearly shown the formation of high-volume-bubble densities [34], with traces of melted-metal droplets of light-Z materials (e.g. aluminium) up to a few meters away from

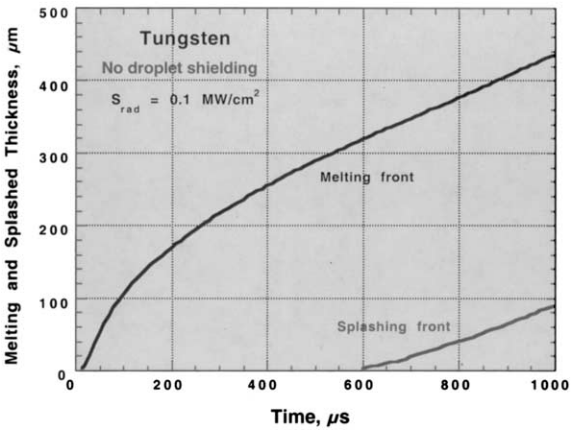

Fig. 10. Time dependence of tungsten melting and splashing front with droplet shielding effect.

the target area. Bubble formation was also found in electron-beam experiments [35]. Careful analysis of the irradiated samples has also suggested the possibility that hydrodynamic instability is a melt-layer erosion mechanism that is in addition to the volume bubble vaporization. Near the central areas of the sample where the velocity of the incident plasma stream along the sample surface is near zero, the volume bubbles are seen clearly. Near the sample peripheral areas, however, one can see liquid droplets with long tracks, formed because of the high velocity of the plasma stream.

Melt-layer erosion of much heavier materials, such as tungsten, was shown to be very low in plasma gun experiments [36] but is more likely to be greater for longer (>1 ms) heat pulse duration. The HEIGHTS package is used to explain this phenomenon in recent plasma-gun disruption simulation experiments. Fig. 10 shows the time dependence of tungsten melting and splashing-erosion depth for a low radiation power level of 0.1 MW cm^{-2} on a tungsten surface without the effect of droplet shielding (anticipated in all laboratory simulation devices). The time τ_{delay} required to heat the surface to a temperature above the splashing condition ($T > T_{\text{vap}}$ [P_{v}], where P_{v} is plasma pressure above the target surface) inversely depends on the square of incoming radiation power.

It was shown that decreasing S_{rad} from 0.3 to 0.1 MW cm^{-2} increases the delay time from 60 to 600 μs, respectively [37]. This finding has two significant implications. The first is that the level of radiation power substantially increases the MP erosion rate (from 100 μm at 0.1 MW cm^{-2} to 900 μm at 0.3 MW cm^{-2}, without droplet shielding). Second, it can explain why in some simulation experiments, particularly with high-Z targets such as tungsten, significant splashing was not seen because the time duration of these simulation devices is short, i.e. less than the time delay required for S_{rad} associated with such experiments. Therefore, to adequately model and simulate the effect of tokamak instability events on erosion lifetime, facilities with a time duration >300 μs is needed. In the VIKA disruption simulation facility [36], it was shown that for different target materials, significant erosion starts after a delay time similar to that predicted by models in HEIGHTS [37].

Therefore, mass losses of divertor plate and nearby components depend strongly on the dynamics and evolution of the vapor cloud and droplets or MPs. The main concern is the time to start ablation and the existence of both vapor and droplet shielding. Mass losses and lifetime of PFMs due to vaporization and ablation depend strongly on interaction conditions that dictate the existence or absence of both vapor cloud and droplet shields. The vapor shield exists if the vapor cloud is well confined by a strong magnetic field. For a divertor plate, the existence of vapor shielding depends on MHD instabilities in the vapor cloud, which can lead to turbulent diffusion across the magnetic field. In an inclined magnetic field, turbulent diffusion leads to vapor flow and loss ('the vapor wind') along the poloidal direction that decreases the efficiency of vapor shielding. The blowing away of droplets or MPs by the vapor wind is more serious because decreasing the droplet shielding significantly enhances droplet emission. For nearby components of the divertor system, existence of shielding depends, in addition, on the geometrical locations relative to magnetic field structure.

Four erosion scenarios are possible during plasma–target interaction [37]. Fig. 11 shows the

erosion depth of both beryllium and graphite targets for these cases with and without both vapor shielding and droplet shielding. In Case 1, i.e. absence of both shielding mechanisms (no vapor shielding, i.e. vapor is not well confined and there is no droplet shielding, so droplets are splashed away from the incoming plasma), all incoming power will be spent in splashing erosion of the liquid surface. Erosion loss is very high, and this case may represent a disruption simulation device in which the incident plasma has a very high dynamic pressure that exceeds the magnetic field pressure that is capable of blowing off the initial vapor cloud and liquid layers. Case 1 may also resemble a tokamak condition in which a strong MHD vapor turbulence develops and leads to fast removal of vapor and droplets along the target surface. In Case 2, without vapor shielding and splashing (or ablation), all incoming power will be spent in vaporizing the target surface. This may occur if the vapor cloud is removed for any reason and the target material does not melt or splash–destruct.

In Case 3, with vapor shielding but without droplet shielding (droplets are removed from incoming power), the net incoming radiation power to the target surface is spent in splashing. This situation can occur on nearby components during a divertor plate disruption, in which the intense photon radiation from the hot vapor cloud deposits its power at locations with different orientations to the magnetic field lines; as a result, the vapor cloud is not well confined. This may also be true in many of the disruption simulation devices, such as plasma guns and electron beams where the cross section of the plasma or particle flow is small and the MPs flight time in the vapor cloud is inadequate to absorb the incoming radiation power and further shield the target surface. This can also occur under tokamak conditions with moderate levels of turbulence, in which the vapor wind is strong enough to blow away droplets but not strong enough to remove all vapor; thus, the remaining vapor cloud has enough depth to stop most incoming plasma particles and radiate back the deposited power. Ablation can increase mass losses by ≈ 4–5 times. Therefore, droplet removal is critical because the result of droplet shielding is that all of the radiation from the vapor cloud goes to the target surface to be spent in vaporization, mostly through the intermediate process of droplet emission and further vaporization during droplet flight across the vapor cloud.

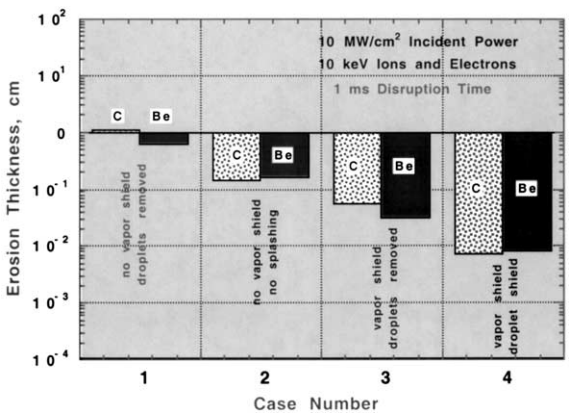

Fig. 11. Erosion depth of berylium and carbon targets for various cases with and without vapor and droplet shielding effects.

The fourth Case is the most desirable and can be realized in a tokamak device if the vapor cloud is well confined and without MHD effects. Under such conditions, a well-confined vapor and droplet cloud can reduce erosion losses by up to two orders of magnitude. It should be noted that these results are valid at longer time $t > \tau_{\text{delay}}$, i.e. when the surface temperature achieves its quasi-stationary value in stable vapor plasma. For shorter times, vaporization losses in the case of vapor and droplet shielding can be calculated directly. However, the liquid droplets or pieces of CBMs, simply stated as MPs, that are ejected near target edges and/or are large or moving with higher velocities will not have sufficient time to completely vaporize and shield the target surface, therefore, erosion lifetime is lower. In addition, higher droplet velocities due to the drag force of the fast-expanding vapor, or due to the high explosive pressure in the brittle destruction mechanism, can increase mass loss because the droplets will spend less time in the hot vapor cloud.

The observed increase in the eroded area, which is larger than the footprint of the incident plasma flow in some simulation experiments, can be ex-

plained as the result of the interaction of vapor radiation with the target surface outside the plasma flow spot [33] or as being due to the developed MHD instabilities in the vapor cloud [20]. In addition, slight shifting of the vapor cloud due to the $[\vec{E} \times \vec{B}]$ force may also occur along the target. However, these problems have not been well investigated and require more analysis and simulation.

To summarize the simulation results, we may say that overheating the plate surface causes MPs and droplets to be ejected–splashed upstream and away from the surface. These particles then absorb some part of the incoming vapor radiation. The net fraction of radiation power that reaches the divertor surface is determined mainly by the ratio of the vaporization to splashing energies. The distance L at which MPs or droplets are completely vaporized is < 1 cm. Therefore, the mixture of vapor and MPs exists only very near the divertor surface. Despite initial large splashing erosion, total erosion of the divertor plate is defined only by vaporization losses, including both divertor plate vaporization and MP vaporization. Again, this is true only if both the vapor cloud and the splashed droplets are well confined in front of the disrupting plasma. However, loss of vapor confinement can occur as a result of the MHD instability that arises from distortion of the oblique magnetic field lines by the expanding vapor plasma [20]. In this case, the developed turbulence leads to vapor flow along the divertor plate surface. Due to this flow, K–H instability of unstable surface waves occurs and leads to splashing.

This vapor flow blows both vapor and droplets along the target surface, reducing vapor shielding efficiency because of vapor cloud removal. In addition, efficiency of droplet shielding is reduced because droplet exposure time in the depleted vapor is decreased. Efficient vapor shielding that protects the divertor plates from high heat loads means that $> 90\%$ of incoming power is radiated to nearby locations. Therefore, the problem of erosion of other parts in a closed divertor system becomes more serious. It was shown both experimentally [28] and theoretically [29] that interaction of this 'secondary' radiation with other components leads to the same consequences as the primary interaction of the SOL plasma, i.e. vapor cloud formation, splashing, etc. Moreover, it may be very difficult for such vapor clouds to be well confined, especially if the magnetic field angle of inclination with variously oriented surfaces is very low. Erosion of such nearby components could be estimated, as done in Case 1 on Fig. 11, because of the absence of both shielding effects.

6. Effects of long-duration plasma instabilities

Thermal-quench disruptions and ELMs have no significant thermal effect on structural materials and coolant channels, because deposition time is short (< 10 ms). However, VDEs (duration 100–300 ms), and runaway electrons (deeper penetration depth), in addition to causing severe surface melting and erosion, can substantially damage these components [2]. One concern is the higher temperature observed in the structural material, particularly at the interface with the coating materials. Elevated temperatures and high thermal stresses in the structure seriously degrade the integrity of the interface bonding; this may lead to detachment of the coating from the structural material.

The surface temperature of the copper-structure during a VDE has been calculated for different surface coated materials such as tungsten, beryllium, and carbon tiles. As an example, Fig. 12 shows the surface temperature of a 5-mm-thick copper substrate at its interface with 5-mm-thick tungsten and beryllium coatings and 20-mm-thick carbon tiles during a typical VDE releasing to the surface about 60 MJ m^{-2} in 300 ms [1]. Under reactor conditions, the tile thickness is determined by the surface temperature limitations during normal operation. With a tungsten coating, the copper surface interface can actually melt. For the given conditions, only beryllium coatings of reasonable thickness (< 5–10 mm) or very thick carbon tiles (> 20 mm) can withstand the acceptable temperature rise in the copper structure, because most of the incident plasma energy is removed by beryllium's higher surface vaporization rate, which leaves little energy to be con-

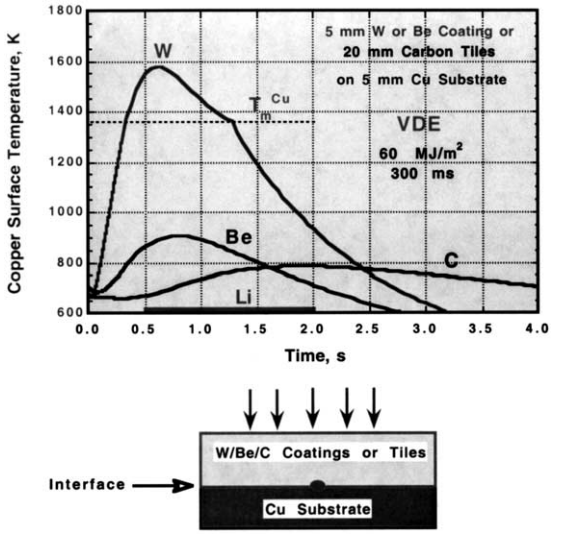

Fig. 12. Time evolution of surface temperature of copper substrate with various surface coating materials.

ducted through the structural material [1]. Therefore, beryllium and carbon coating materials will suffer significant surface erosion while protecting the structural copper substrate. A thin (≈ 1–2-cm-thick) free-surface layer of a liquid metal such as lithium would be ideal to completely protect the structure and offer unlimited PFC erosion lifetime. Lithium is shown in Fig. 12 only for comparison. The temperature rise in copper structure is very small when lithium is used. The structural materials will, therefore, exhibit no high-temperature effects during the VDE because the liquid metal will remove the heat by either convection (moving film) or intense vaporization (stationary film). However, problems related to plasma–free-surface liquid–metal interactions during normal operations must be carefully examined.

7. Summary and conclusions

Mechanisms of material erosion and lifetime during plasma disruptions are modeled in detail. Erosion of plasma-facing materials is governed by both the characteristics and distribution of incident plasma particles from the SOL, as well as by processes that lead to vapor and droplet formation and shielding. Two separate mechanisms of material erosion occur during plasma disruptions, atomic vaporization from the target surface and ablation in the form of MPs (i.e. liquid metal droplets or macroscopic pieces of CBMs). Ablation can be attributed to hydrodynamic instabilities, volume-bubble boiling (metallic materials), thermal stresses, and pore explosion (brittle materials), A HEIGHTS-package numerical simulation was carried out with new models for dynamic evolution and interaction of MPs with an inhomogeneous vapor cloud.

The ablation mechanism plays a more important role because the required threshold energy needed for ablation is much less than the energy of vaporization. It can lead to significant mass losses if the ejected MPs are removed quickly before they are completely vaporized. In the absence of strong plasma and vapor wind or vapor turbulence diffusion, a new process, named 'droplet shielding', takes place and leads to significant reduction in total mass losses from the target surface. The shielding efficiency of both vapor and droplet shielding in well-confined vapor plasma can exceed 95% for candidate materials like lithium, beryllium, and carbon.

In a typical disruption of an ITER-like machine, of $\tau_d \approx 1$ ms; the predicted mass losses per disruption are on the order of $X_{loss}(\mathrm{Li}) \approx 750$ μm, $X_{loss}(\mathrm{Be}) \approx 30$ μm, and $X_{loss}(\mathrm{C}) \approx 22$ μm. These values may seem acceptable from an engineering point of view; however, one should note that all of the above analyses assumed no vapor–plasma wind or turbulence diffusion along the divertor plate surface. In such a case, the actual erosion values of the divertor plate and nearby components will be significantly increased. In addition, the deposition of eroded and splashed materials on reactor components can adversely affect plasma performance. The use of a renewable material such as free-surface liquid lithium may significantly extend the lifetime of PFMs and substantially enhance the tokamak concept for power-producing reactors. In general, major plasma instabilities must be avoided or their frequency be significantly reduced.

Acknowledgements

Work is supported by the US Department of Energy, Office of Fusion Energy, under Contract W-31-109-Eng-38.

References

[1] A. Hassanein, I. Konkashbaev, Fusion Eng. Des. 51–52 (2000) 681.
[2] A. Hassanein, Fusion Technol. 30 (1996) 713.
[3] A. Hassanein, G. Federici, et al., Fusion Eng. Des. 39–40 (1998) 201.
[4] A. Hassanein, I. Konkashbaev, J. Nucl. Mater. 273 (2000) 326.
[5] A. Hassanein, I. Konkashbaev, "Physics of collisionless scrape-off-layer plasma during normal and off-normal tokamak operating conditions," Argonne National Laboratory Report ANL/FPP/TM-296, March 1999.
[6] A. Hassanein, I. Konkashbaev, Suppl. J. Nucl. Fusion 5 (1994) 193.
[7] A. Hassanein, I. Konkashbaev, J. Nucl. Mater. 290–293 (2001) 1074.
[8] A. Hassanein, V. Belan, et al., J. Nucl. Mater. 241–243 (1997) 288.
[9] A. Hassanein, Response of Materials to High Heat Fluxes during Operation in Fusion Reactors, ASME, 1998 88-WA/NE-2.
[10] A. Hassanein, Fusion Technol. 15 (1989) 513.
[11] A. Hassanein, et al., in: K. Herschbach, W. Maurer, J.E. Vetter (Eds.), Fusion Technology, 1994, p. 223.
[12] A. Hassanein, I. Konkashbaev, Fusion Eng. Des. 28 (1995) 27.
[13] A. Hassanein, I. Konkashbaev, Plasma Devices Operations 5 (1998) 297.
[14] L.L. Lengyel, et al., Nucl. Fusion 36 (1996) 1679.
[15] L.L. Lengyel, V.A. Rozhansky, J.Yu. Veselova, Drift motion in the scrape-off-layer during hard disruptions, Proceedings 24th European Physical Society Conf. on Contr. Fus. and Plasma Phys., (Berchtesgaden, Germany, 1997), Ed. Eur. Phys. Soc., Geneva, Vol. 21A-pan 4, 1997 1549.
[16] I.S. Landman, H. Wuerz, Electric stopping in hot-plasma-wall interactions, Proceedings 24th European Physical Society Conf. on Contr. Fus. and Plasma Phys., (Berchtesgaden, Germany, 1997), Ed. Eur. Phys. Soc., Geneva, Vol. 21A-part 4, 1997 1821.
[17] R. Vassen, A. Kaiser, D. Stover, J. Nucl. Mater. 233–237 (1996) 713.
[18] S. Pestchanyi, N. Usov, H. Wuerz, Numerical simulation of brittle destruction of carbon-based materials due to pulse plasma heating, Proceedings 20th Symp. Fus. Technol. (Marseille, France, 1998), Beaumont, B., et al. (Eds.), Vol. 1, 1998 275.
[19] M. Guseva, et al., J. Tech. Phys. 66 (6) (1966) 106.
[20] A. Hassanein, I. Konkashbaev, J. Nucl. Mater. 258–263 (1998) 645.
[21] A. Hassanein, Effect of Macroscopic Eroded Debris on Lifetimes of Plasma-Facing Components during Plasma Instabilities, presented at 21st European Symposium on Fusion Technology (SOFT), 11–18 September 2000, Madrid, Spain. Accepted for publication in Fusion Eng. Des. 56–57 (2001) 409.
[22] V. Belan, et al., J. Nucl. Mater. 233–237 (1996) 763.
[23] V. Litunovsky, et al., in: B. Beaumont, P. Libeyre, B. de Gentile, G. Tonon (Eds.), Fusion Technology, 1998, p. 59.
[24] N.I. Arkhipov, et al., J. Nucl. Mater. 233–237 (1996) 767.
[25] J. Linke, et al., in: B. Keen, M. Huguet, R. Hemsworth (Eds.), Fusion Technology, 1991, p. 428.
[26] J. Van der laan, J. Nucl. Mater. 162–164 (1989) 964.
[27] A.V. Burdakov, et al., J. Nucl. Mater. 233–237 (1996) 697.
[28] V. Safronov, N. Arkhipov, et al., in: B. Beaumont, P. Libeyre, B. de Gentile, G. Tonon (Eds.), Fusion Technology, 1998, p. 105.
[29] A. Hassanein, I. Konkashbaev, in: C. Varandas, F. Serra (Eds.), Fusion Technology, 1996, p. 379.
[30] Y.V. Martynenko, et al., J. Nucl. Mater. 258–263 (1998) 1120.
[31] V. Safronov, et al., J. Nucl. Mater. 290–293 (2001) xxx.
[32] V. Belan, et al., J. Nucl. Mater. 233–237 (1996) 763.
[33] A. Hassanein, I. Konkashbaev, Disruption simulation experiments and extrapolation to reactor conditions, Proc. 20th Symp. Fusion Technology (Marseille, France, 1998), B. Beaumont, et al. (Eds.) Vol. 1, 1998 245.
[34] N.I. Arkhipov, V.P. Bakhtin, V.M. Safronov, D.A. Toporkov, S.G. Vasenin, H. Wurz, A.M. Zhitlukhin, Plasma temperature measurements in disruption simulated experiments, in: K. Herschbach, W. Maurer, J.E. Vetter (Eds.), Proceedings 18th Symposium Fusion Technology, (Karlsruhe, Germany, 1994), vol. 1, Elsevier, Amsterdam, 1995, p. 395.
[35] A.V. Burdakov, et al., J. Nucl. Mater. 233–237 (1996) 697.
[36] V. Litunovsky et al., Proceedings 20th Symposium on Fusion Technology (SOFT), 7–11 September, Marseille, France, Vol. 1, 1998 59.
[37] A. Hassanein, I. Konkashbaev, J. Nucl. Mater. 290–293 (2000) 1171.